remote sensing

MDPI

Article

A Novel Method for Simplifying the Distribution Envelope of Green Tide for Fast Drift Prediction in the Yellow Sea, China

Yi Ding [1,2,3], Song Gao [1,2], Guoman Huang [3,4,*], Lingjuan Wu [1,2], Zhiyong Wang [3], Chao Yuan [1,2] and Zhigang Yu [3]

1 North China Sea Marine Forecasting and Hazard Mitigation Center, Ministry of Natural Resources, Qingdao 266061, China
2 Shandong Provincial Key Laboratory of Marine Ecology and Environment & Disaster Prevention and Mitigation, Qingdao 266061, China
3 College of Geodesy and Geomatics, Shandong University of Science and Technology, Qingdao 266590, China; skd994177@sdust.edu.cn (Z.W.); yu_zg@sdust.edu.cn (Z.Y.)
4 Institute of Photogrammetry and Remote Sensing, Chinese Academy of Surveying and Mapping, Beijing 100036, China
* Correspondence: huang.guoman@casm.ac.cn; Tel.: +86-1063880808

Abstract: Since 2008, annual outbreaks of green tides in the Yellow Sea have had severe impacts on tourism, fisheries, water sports, and marine ecology, necessitating effective interception and removal measures. Satellite remote sensing has emerged as a promising tool for monitoring large-scale green tides due to its wide coverage and instantaneous imaging capabilities. Additionally, drift prediction techniques can forecast the location of future green tides based on remote sensing monitoring information. This monitoring and prediction information is crucial for developing an effective plan to intercept and remove green tides. One key aspect of this monitoring information is the green tide distribution envelope, which can be generated automatically and quickly using buffer analysis methods. However, this method produces a large number of envelope vertices, resulting in significant computational burden during prediction calculations. To address this issue, this paper proposes a simplification method based on azimuth difference and side length (SM-ADSL). Compared to the isometric and Douglas–Peucker methods with the same simplification rate, SM-ADSL exhibits better performance in preserving shape and area. The simplified distribution envelope can shorten prediction times and enhance the efficiency of emergency decision-making for green tide disasters.

Keywords: green tide; satellite remote sensing; distribution envelope; buffer analysis; simplification method

Citation: Ding, Y.; Gao, S.; Huang, G.; Wu, L.; Wang, Z.; Yuan, C.; Yu, Z. A Novel Method for Simplifying the Distribution Envelope of Green Tide for Fast Drift Prediction in the Yellow Sea, China. *Remote Sens.* **2024**, *16*, 3520. https://doi.org/10.3390/rs16183520

Academic Editor: Hatim Sharif

Received: 27 August 2024
Revised: 18 September 2024
Accepted: 18 September 2024
Published: 23 September 2024

1. Introduction

Since the large-scale outbreak in 2008 [1–7], the green tide in the Yellow Sea has occurred annually. Through years of monitoring, the process of green tides is usually divided into five stages: occurrence, development, outbreak, decline, and extinction [4–8]. Each year, the green tide originates from the radial sandbanks in northern Jiangsu in early May and drifts northward under the influence of wind and ocean currents. The green tide reaches its maximum scale in the waters near the southern coast of Shandong around late June or early July. From early to mid-July, the green tide begins to decline and gradually disappears in mid-to-late August. As the green tide drifts from south to north and east, it causes varying degrees of harm to aquaculture, water sports, tourism and marine ecology [4–11]. Therefore, the Marine Management Department of the area affected by the disaster expends a lot of workforce and material resources in preventing and eliminating the green tide disaster [3–5].

Satellite remote sensing, with its wide range and advantage of instantaneous data acquisition, has become the primary data resource for monitoring green tides in the Yellow

Sea and the only way to obtain complete green tide information [2–8,12,13]. Satellite remote sensing typically employs vegetation indices to extract green tide information. Vegetation indices effectively enhance vegetation information while mitigating interferences from imaging angles, solar glare, the atmosphere, and other factors. Commonly used indices include the Normalized Difference Vegetation Index (NDVI) [2,8,12], Normalized Difference Algae Index (NDAI) [14], Floating Algae Index (FAI) [15], Scaled Algae Index (SAI), Index of floating Green Algae for GOCI (IGAG) [16], Virtual-Baseline Floating macroAlgae Height (VB-FAH) [17], and Multispectral Green Tide Index (MGTI) [18]. Among these, the NDVI only requires two bands, red and near-infrared, making it applicable to all satellite imagery and the most widely used in operational applications and green tide research. During green tide satellite remote sensing emergency monitoring, firstly, satellite imagery is used to detect the green tide patches, and then, patches are used to produce the distribution envelope [2,5,12]. Finally, the distribution envelope vertices are used as the initial field for predicting the drift of the green tide [19–22]. Based on the monitoring and drift prediction results, disaster management plans are determined [22,23]. The main disaster management methods include ship-based removal, fence-based blocking, and coastal cleanup.

At present, the distribution envelope of green tide can be delineated by manual interpretation [2,24] or computer analysis based on the green tide patches [25]. The manual interpretation option has the following advantages: the quantity of distribution envelope vertices is moderate, they can be directly used as the initial field, and predicting drift requires only a short calculation. The weaknesses of this method include intense subjectivity, a lack of uniform standards, and the fact that different scientists analyzing the same green tide patches will draw different distribution envelopes. The second option (computer analysis) uses the buffer analysis method. The buffer analysis tool of ArcGIS is usually applied to form a green tide distribution envelope by buffering the green tide patches [25]. The distribution envelope formed by this method is automatic and standard. However, the number of distribution envelope vertices often reaches tens or hundreds of thousands. Due to the high computational pressure, they cannot be used directly as initial fields for drift prediction and must be simplified. A simplification method for polygons created by buffer analysis has not yet been reported.

Existing polygon simplification models include the equidistance method, the ray-barrier method, the vertical distance tolerance method, and the Douglas–Peucker method [26–29]. The equidistance method selects vertices by setting a fixed side length between them. The ray-barrier method achieves vertex selection by setting the angle threshold between adjacent sides, which is not suitable for polygons with uniform distribution of vertex angles. The vertical distance tolerance method achieves simplification by controlling the vertical distance between simplified and original envelopes, which is a local algorithm and not suitable for envelopes with little different side lengths and vertex angles. The Douglas–Peucker algorithm is an improved version of the vertical distance tolerance method, and is a global algorithm rather than a local algorithm. The above methods have their respective advantages, weaknesses, and applicability. They are all designed to simplify geographic information data, such as administrative boundaries and contour lines [28,30,31]. The feasibility of simplifying polygons formed by buffer analysis using the above methods has not been evaluated.

The objective of this study was to develop a simplification model of the distribution envelope formed by buffer analysis. The model obtained in this paper can effectively simplify the distribution envelope vertices, reducing the calculation pressure associated with drift prediction and improving the efficiency of green tide disaster emergency decision-making. The paper is organized as follows: Section 2 describes the study area, as well as the data and their processing. Section 3 proposes the method for building a simplification model and model assessment. Section 4 presents the simplification model, precision evaluation and applications. Section 5 gives the simplified envelopes analysis, methods comparison analysis, and drift prediction analysis. Section 6 includes the conclusions.

2. Study Area and Data

2.1. Study Area

The study area was the southern region of the Yellow Sea (see Figure 1), where the north wind prevails in winter, and the south wind prevails in summer. Due to wind effects, the area's sea surface current shows the same mode, flowing from south to north in summer [32]. This area experiences semi-diurnal tides, with a greater tidal range in the east than in the west. At the same time, the semi-diurnal tidal currents in this region are pronounced, and the flow velocity in the east is greater than that in the west [33,34]. The western part of this area includes the Subei radiation shoal, which due to unique geological and tidal conditions, provides a favorable environment for the growth of Porphyra yezoensis. This area has become a well-known area for the aquaculture of Porphyra yezoensis [35]. Porphyra rafts offer conditions for the adhesion and growth of green tide algae [36,37]. During the harvesting of Porphyra yezoensis in late April and early May, green tide algae are abandoned into the sea from the culture rafts and become the primary source of the green tide. They continue to grow and drift northward under favorable oceanographic conditions (temperature, wind and current) for the transportation and rapid growth of the Enteromorpha prolifera bloom [3,38,39]. Eventually, the green tide reaches the waters of Shandong Province (to the north of the study area) and sinks to the bottom of the sea off southern Shandong Province in late June or early July, causing damage to local fisheries, water sports, tourism, and marine ecology.

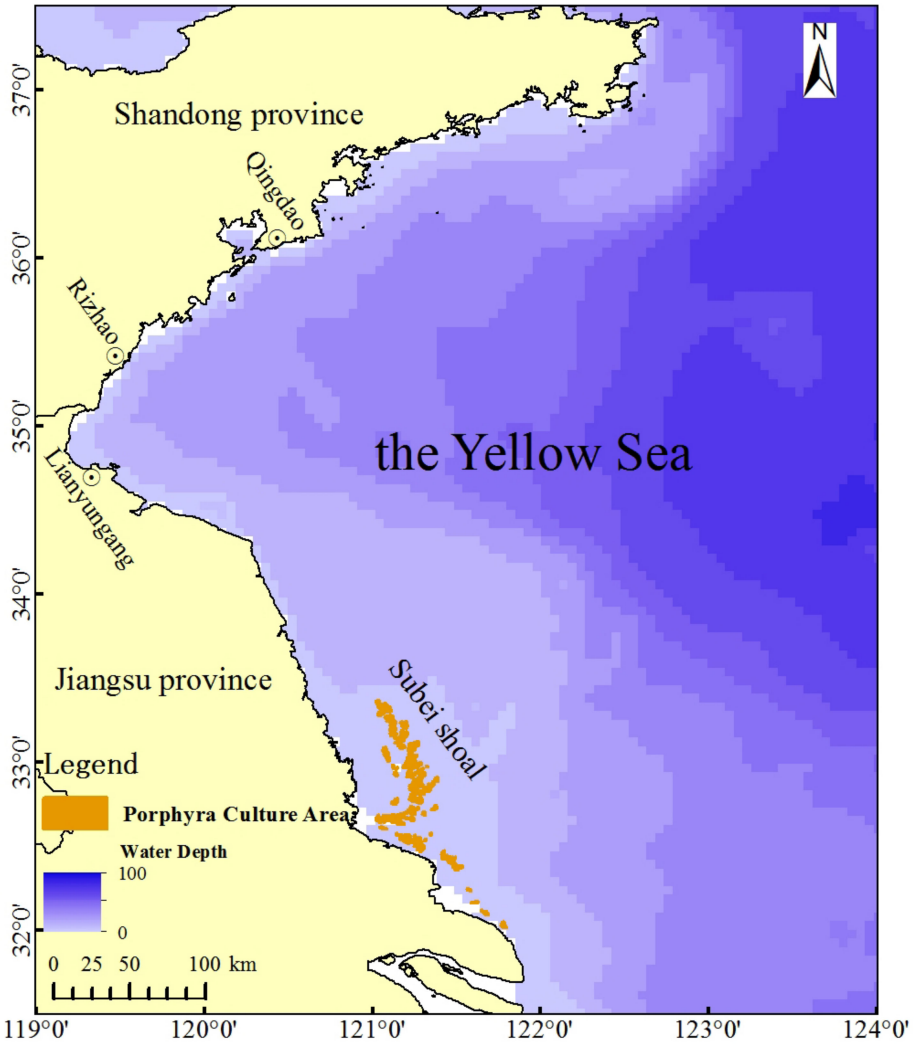

Figure 1. Schematic diagram of study area.

2.2. Data and Data Processing

2.2.1. Satellite Data

The HaiYang-1D satellite (HY-1D), launched on 11 June 2020, operates as a dual-satellite network with HaiYang-1C (HY-1C). Together, they can capture a full view of the green tide in the Yellow Sea twice every three days with a spatial resolution of 50 m and a scanning range of 950 km. The Coastal Zone Imager (CZI) on satellite HY-1C/D contains four wavebands for effective green tide monitoring: blue (0.42–0.50 μm), green (0.52–0.60 μm), red (0.61–0.69 μm), and near-infrared (0.76–0.89 μm) [40]. Since 2019, this imagery has been one of the primary satellite resources for green tide monitoring in the Yellow Sea. Eight HY-1C/D satellite images from 2021 were used in this study (see Table 1).

Table 1. Information on satellite images used for green tide monitoring in this paper.

Satellite/Sensor	Date	Object	Stage
HY-1C/CZI HJ-2B/CCD	10 May 2021	Process analysis, comparative analysis	Emergence
HY-1D/CZI	17 May 2021	Algorithm development, application, validation, comparative analysis, and process analysis	Development
HY-1C/CZI	25 May 2021	Process analysis	Development
HY-1D/CZI HJ-2A/CCD	6 June 2021	Algorithm application, validation, comparative analysis, and process analysis	Explosion
HY-1C/CZI	9 July 2021	Algorithm application, validation, comparative analysis, and process analysis	Explosion
HY-1C/CZI	18 July 2021	Process analysis	Decline
HY-1C/CZI	5 August 2021	Algorithm application, validation, comparative analysis, and process analysis	Decline
HY-1C/CZI	25 August 2021	Process analysis	Extinction

The Huanjing-2 A/B Satellites (HJ-2A/B) were successfully launched on 27 September 2020. Each satellite has four types of optical payloads: a 16 m camera, a hyperspectral imager, an infrared camera, and an atmospheric corrector. The 16 m camera payload consists of four visible CCD cameras that cover the blue, green, red, red edge, and near-infrared bands, each with a single width exceeding 200 km. By mosaicing the fields of view, it can provide multispectral images with a width of 800 km [41]. The two satellites, networked in the same orbit, can quickly acquire imagery and can cover the green tide area with visible and infrared multispectral data once every two days, serving as a valuable supplementary data source for HY-1C/D satellites. Two HJ-2A/B satellite images from 2021 were used in this study (see Table 1).

2.2.2. Green Tide Extraction

The normalized difference vegetation index (NDVI), which is calculated using Formula (1) based on the unique spectral characteristics of green algae in the red and near-infrared bands, is widely applied in the extraction of green tides [2,4,6–8,12,42–44]. The optical satellite images used in green tide monitoring all have red-light bands and near-infrared bands. Therefore, this paper applies the NDVI threshold method to extract green tide information. From April to July every year, the Yellow Sea is cloudy and foggy [45,46], which seriously affects the monitoring of green tide. Therefore, we designed a green tide information extraction process combining visual and automatic processes to reduce the influence of cloud and sea fog on green tide extraction (see Figure 2). First, a standard

false-color image combined with NDVI is used to visually identify the green tide area, which can effectively eliminate interference factors such as clouds and fog. Next, the NDVI threshold method is used to extract the green tide in the green tide area. Under normal conditions, the NDVI threshold is 0 and can be slightly adjusted regarding the extraction effect of green tide.

$$\mathrm{NDVI} = (\mathrm{Rnir} - \mathrm{Rred})/(\mathrm{Rnir} + \mathrm{Rred}) \quad (1)$$

where Rnir and Rred denote the reflectance in near-infrared and red wavebands, respectively.

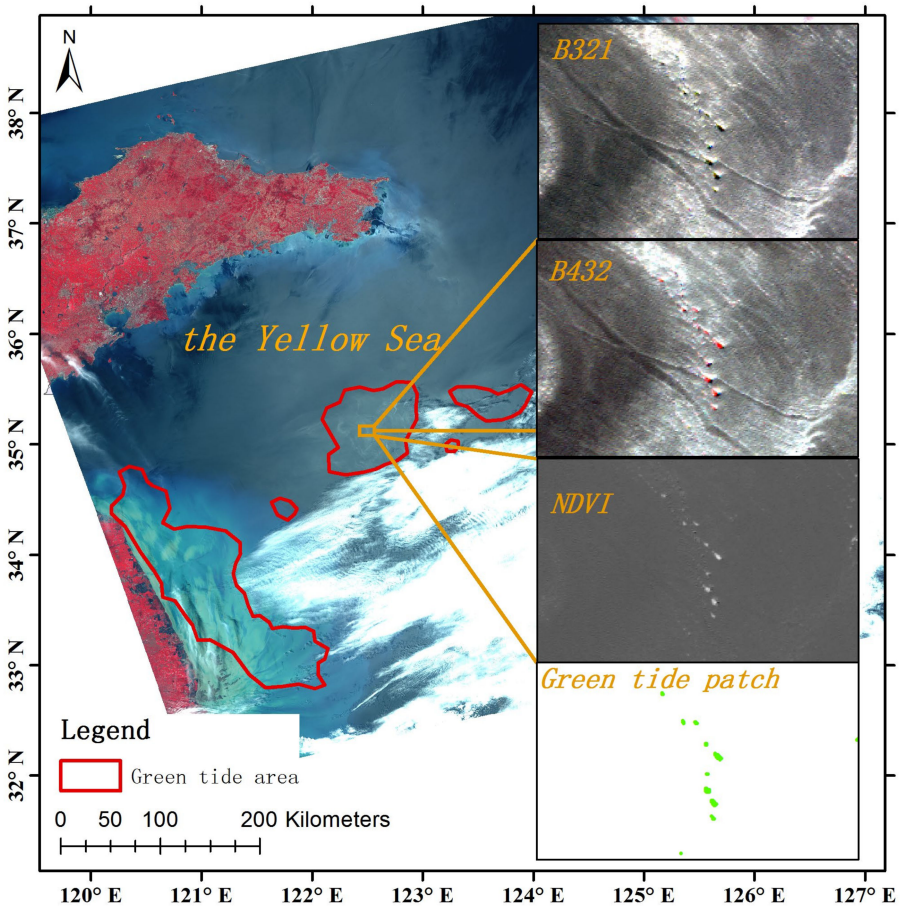

Figure 2. Schematic diagram of green tide information extraction on 17 May 2021. The green tide area outlined in red was obtained by visual interpretation based on standard false color image B432 (R-nir, G-red, B-green), which has a higher contrast than true color image B321 for green tide, and green tide patches shown in green that were obtained by the NDVI threshold method.

2.2.3. Side Lengths and Vertex Angles of the Envelope

The buffer analysis tool in ArcGIS desktop 10.6 software was used to create green tide distribution envelopes based on green tide patches. Based on field monitoring, there are meter-scale and sub-meter-scale patches surrounding the large patches. In operational monitoring, the primary satellite source, HY-1, has a spatial resolution of 50 m, making it difficult to detect these smaller patches. Additionally, there are errors in drift prediction. To ensure that smaller patches around the bigger patches are not omitted during an emergency response, we set the buffer radius to 3 km in the buffer analysis. It is well-known that buffer analysis can form an envelope with smooth boundaries. We calculated the side lengths and angles on the distribution surface of 17 May 2021 as an example. Figure 3 shows that the angles were all greater than 175 degrees, concentrated between 178 and 180 degrees, and the side lengths were all less than 0.2 km, mostly within 0–0.1 km. The characteristics of the side lengths and angles corroborated the smooth boundary characteristics of the

envelope. Therefore, the ray-barrier method and the vertical distance tolerance method are not suitable for the distribution envelope formed by the buffer analysis.

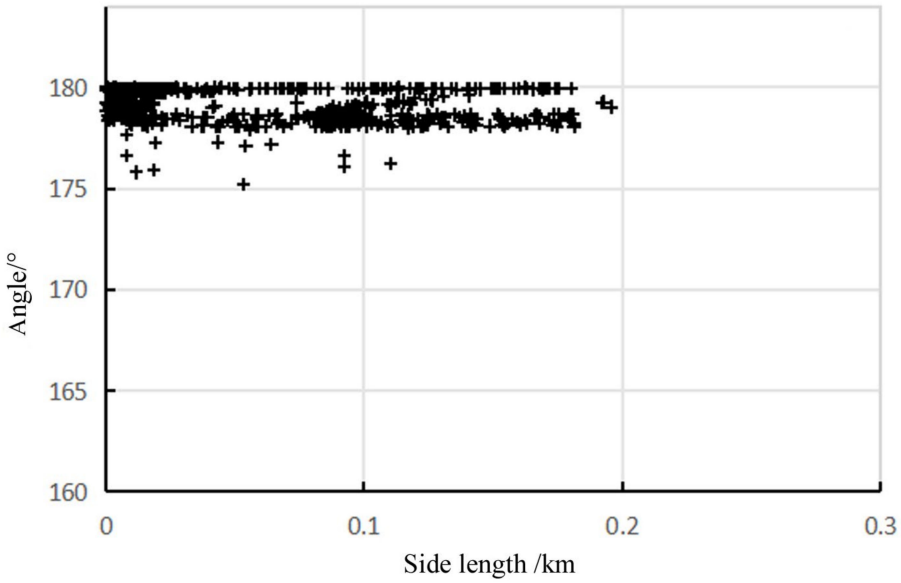

Figure 3. Side lengths and angles of green tide distribution envelope on 17 May 2021.

3. Method

3.1. Method for Building Simplification Model

As seen in Section 2.2.3 above, the buffer-formed distribution envelope has the characteristics of small side lengths and large vertex angles, resulting in many redundant points. Increasing the side length of the envelope surface can effectively eliminate redundancy, thereby compressing the boundary vertices. At the same time, to effectively maintain the shape of the envelope surface after simplification, different side lengths should be applied in flat boundary areas and areas with high curvature. Therefore, we firstly manually selected the sample vertices from the original distribution envelope vertices, and secondly, analyzed the characteristics of azimuth differences and side lengths of adjacent sample vertices. We then established the simplification model by applying statistical methods based the above two factors.

3.2. Accuracy Assessment

3.2.1. Simplification Error

Distribution envelope simplification can lead to deformation and area change. The overall error (OE) takes into account both the increase and decrease in the deformation compared to the original distribution envelope. Therefore, the overall error was adopted to evaluate the deformation error. The OE formula is as follows:

$$OE = (S_i + S_d)/S_0, \quad (2)$$

where S_0, S_i, and S_d denote the areas of the original envelope, and the increased and decreased parts of the simplified envelope, respectively.

The algebraic error (AE) is the ratio of the area difference between the simplified and the original envelope to the original envelope area, and can be used to evaluate the area change. The AE formula is as follows:

$$AE = (S - S_0)/S_0, \quad (3)$$

where S_0 and S denote the areas of the original and simplified envelope, respectively.

3.2.2. Simplification Rate

The simplification rate was used to evaluate the simplification degree of an envelope, which is the number of original envelope vertices divided by the number of simplified envelope vertices, using the formula $Sr = N_{ori}/N_{sim}$, where Sr, N_{ori}, and N_{sim} denote the simplification rate, the vertex number of the original envelope, and the vertex number of the simplified envelope, respectively.

4. Results

4.1. Simplification Model Based on Azimuth Difference and Side Length (SM-ADSL)

4.1.1. Manually Simplifying the Envelope

The selection of distribution envelope simplification samples followed two principles. First, to obtain a high simplification ratio, the sample vertices selected should be as few as possible. Second, to reduce the simplification error, the line segment between adjacent sample vertices should have a small deformation to the original envelope. These two principles are contradictory because a large simplification rate requires a long side length between sample vertices, which increases deformation and generates a large simplification error. Therefore, during sample selection, it is necessary to balance the above two principles and focus on envelope areas with large or small curvature. For a boundary with low curvature, the side length between adjacent sample points should be as long as possible to enhance the simplification rate. For a part of an envelope with high curvature, the deformation between the original and simplified envelope should be mainly focused on reducing the simplification error. Figure 4A shows a part of the envelope with low curvature. Points a_0 and a_1 are adjacent sample vertices with a longer side length. Figure 4B shows a part of the envelope with high curvature. Points b_0, b_1, and b_2 are the adjacent sample vertices with shorter side lengths.

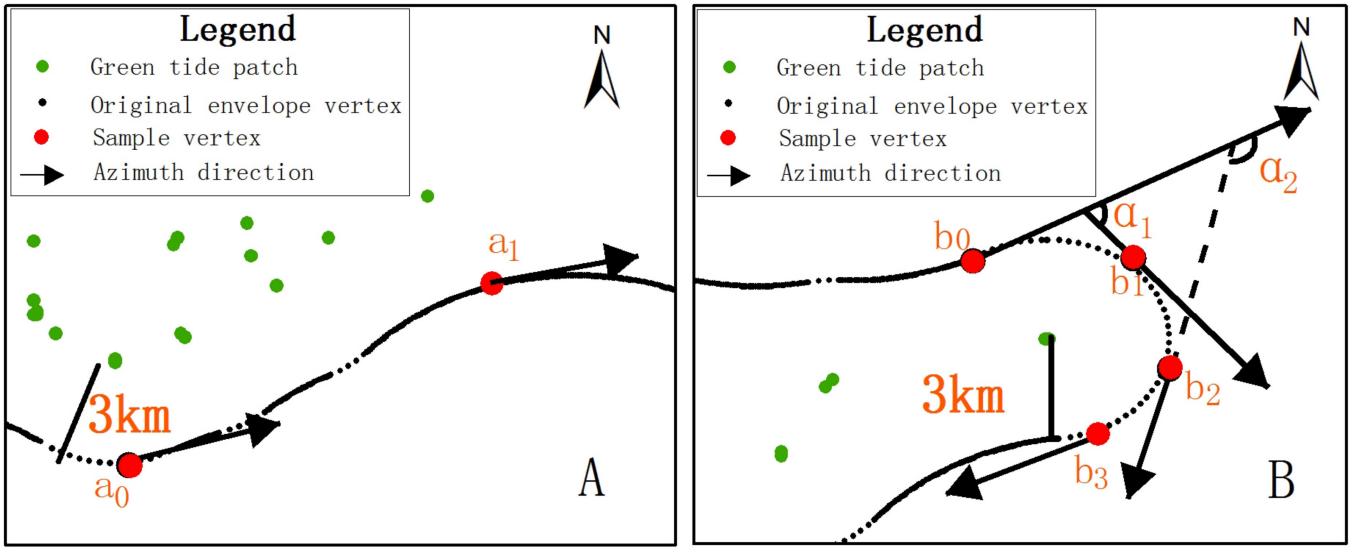

Figure 4. Schematic diagram of sample vertices selection in parts of an envelope with (**A**) low curvature and (**B**) high curvature. The ray directions are the azimuth directions of the vertices connected to them, and α_1 and α_2 are the azimuth differences of the vertices b_0b_1 and b_1b_2, respectively.

Taking the green tide distribution envelope in 17 May 2021 as an example, there were 56,763 vertices in the original distribution envelope. According to the two principles introduced above, we selected 177 vertices with a simplification rate of 196. Figure 5 shows that the hand-selected vertices are a good representation of the original envelope shape.

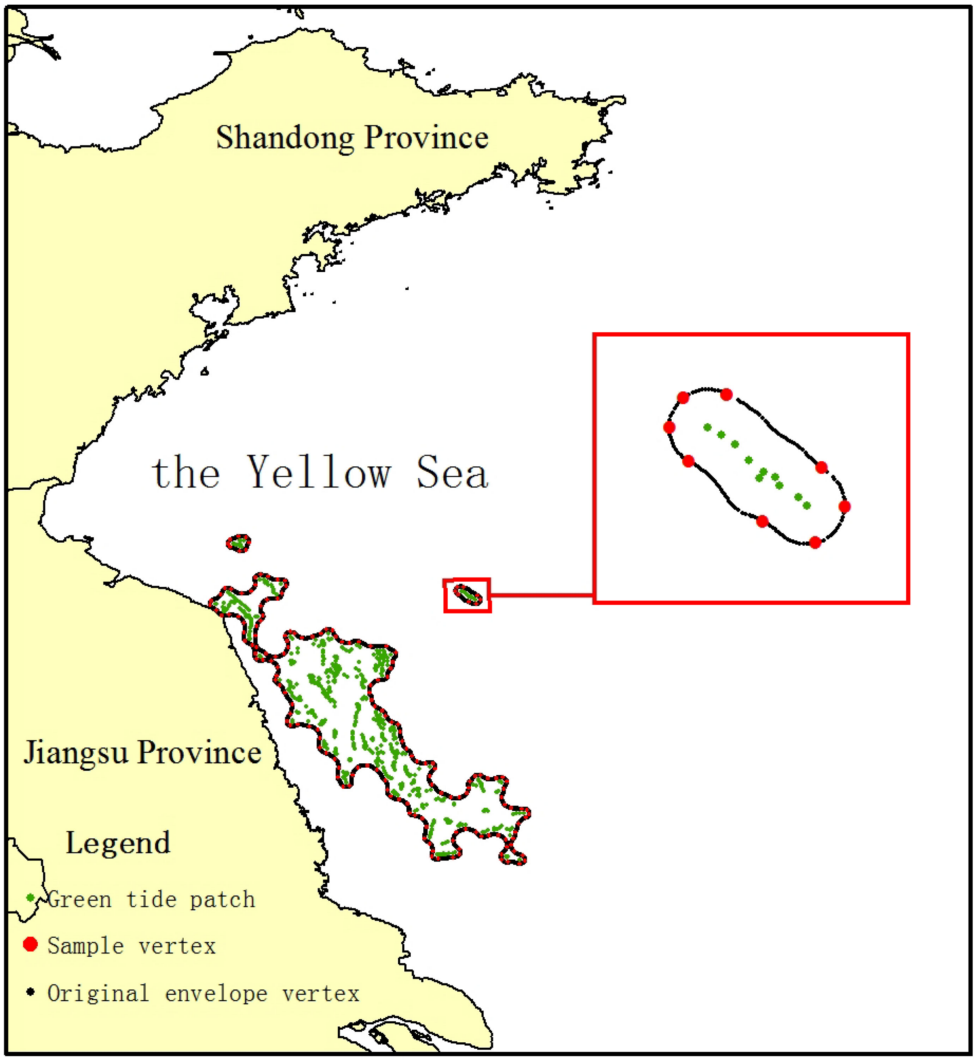

Figure 5. Schematic diagram of sample vertices selection in green tide distribution envelope on 17 May 2021.

4.1.2. Building the Simplification Model

Based on the two principles of sample vertex selection, we identified two characteristics. The first was the side length between adjacent sample vertices, which determined the simplification rate, such as side lengths a_0a_1 and b_0b_1 in Figure 4. The second was the azimuth difference between adjacent sample vertices, which determined the deformation between the original and simplified envelopes. The azimuth of a vertex is defined as the direction of the ray passing through that vertex, which is tangent to the distribution envelope and biased towards the next vertex to be selected. For example, the ray starting at b_0 in Figure 4B is the azimuth of b_0, and angle α_1 is the azimuth difference between the two selected vertices b_0 and b_1.

Applying the 177 sample vertices on the distribution envelope on 17 May, we calculated the azimuth differences and side lengths of adjacent vertices. Figure 6 is the scatter plot of the sample vertices, where the x-coordinate is the azimuth difference, and the y-coordinate is the side length. The following two rules can be discerned: (1) When the azimuth difference varies between 0 and 60°, there is a negative correlation between azimuth difference and side length in general, and almost all side lengths are larger than 3 km. (2) When the azimuth difference is larger than 60°, the corresponding side length varies between 3 km and 4 km.

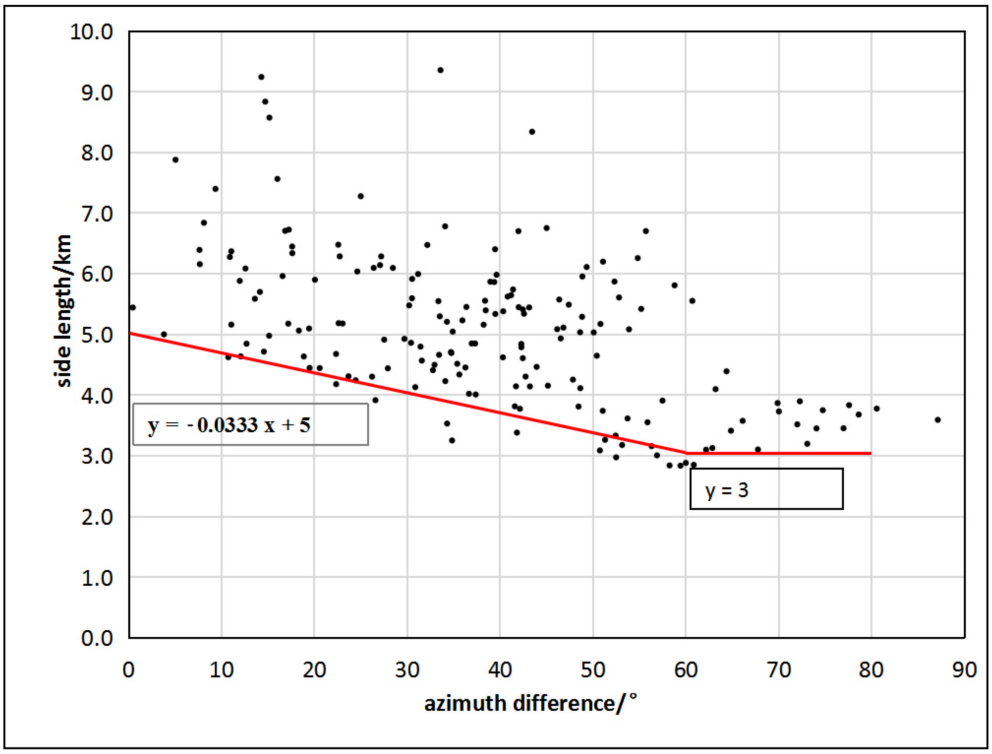

Figure 6. Azimuth difference and side length of adjacent sample vertices (x and y represent the azimuth difference and the corresponding side-length minimum, respectively).

The smaller the side length between the adjacent sample vertices, the smaller the deformation and area change between the simplified and the original distribution envelope. Therefore, we used the azimuth difference of the sample and the corresponding minimum side length to establish a simplification model (see Figure 6), which can ensure that the error of the simplified result is smaller than that of samples. The distribution envelope simplification formula was determined as follows:

$$y = \begin{cases} -0.0333\,x + 5, & x \leq 60^\circ \\ 3, & 60^\circ < x \leq 80^\circ \end{cases}, \quad (4)$$

where x indicates the absolute value of the azimuth difference between adjacent vertices, and y indicates the corresponding side length in the distribution envelope.

4.2. Model Application Process

The flow chart in Figure 7 illustrates the process of mapping the green tide distribution and its drift prediction initial field. It shows three steps: First, the green tide coverage information was extracted, which includes NDVI calculation from the satellite image and the green tide pixels extraction using the NDVI threshold value method. Second, the green tide distribution was mapped through buffer analysis based on the coverage information; and third, the initial field of drift prediction was mapped using the developed simplification method. The distribution usually contained several polygons. We simplified the polygons in the order of the ID number in the SHP file. Each polygon simplification process was as follows: First, we selected the NO.1 vertex as the current vertex and calculated the side-length and azimuth difference between the next vertex. Then, the next vertex was judged to be selected or not according to the simplification algorithm developed. It became the current vertex if selected, and the process was repeated until all the vertices of the polygon were judged.

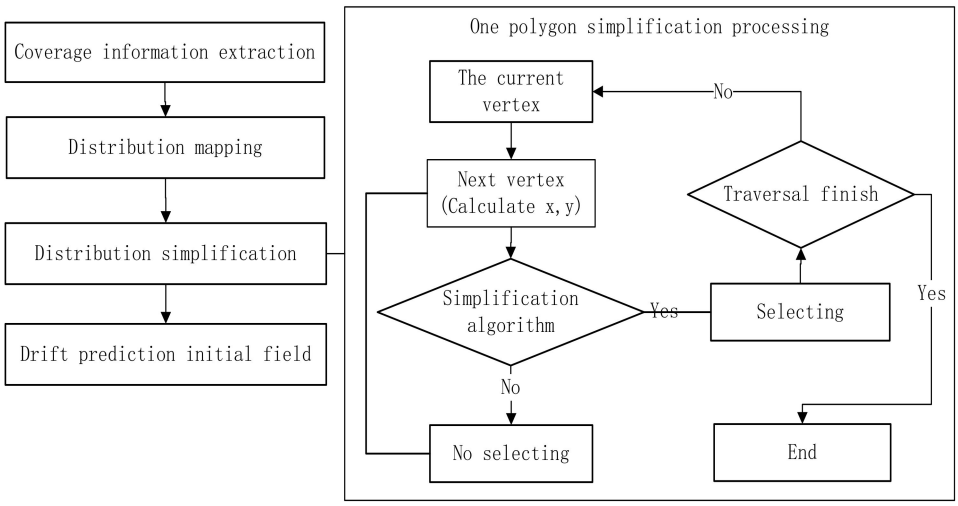

Figure 7. Mapping flow chart of green tide distribution and drift prediction initial field (x and y represent the azimuth difference and side length, respectively).

Azimuth difference x refers to the absolute value of the azimuth difference between the currently selected vertex and the candidate vertex. There are four situations encountered in the calculation of azimuth difference: (1) When the azimuth of the candidate vertex changes in the direction of increase, the azimuth difference $x = x_2 - x_1$. (2) If the azimuth of the candidate vertex is close to 360° and crosses 360° during iteration, the azimuth difference is $x = x_2 - x_1 + 360°$. (3) When the azimuth of the candidate vertex changes in the direction of decrease, the azimuth difference $x = x_1 - x_2$. (4) If the azimuth decreases to 0° and crosses 0° during iteration, the azimuth difference $x = x_1 - x_2 + 360°$. Here, x_2 represents the azimuth of the candidate vertex, and x_1 represents the azimuth of the previously selected vertex.

4.3. Simplification Model Evaluation

The four distribution envelopes for 17 May, 6 June, 9 July, and 5 August 2021 were simplified based on the SM-ADSL. The simplified distribution envelopes are shown in red in Figure 8, which have very little deformation compared to the original envelops shown in black.

The number of original envelope vertices (NOEV), number of simplified envelope vertices (NSEV), area of the original distribution envelope (AODE), and area of the simplified distribution envelope (ASDE) were calculated (see Table 2). The simplification rate, overall error, and algebraic error were calculated based on the evaluation methods in Section 3.2.1. The results are shown in Table 2. Overall, the simplification rates for these four dates were higher than 150, the overall errors were less than 0.75%, and the absolute values of algebraic errors were less than 0.13%.

Table 2. Simplification rate and errors of the simplified envelope produced by this method.

Date	Vertex Number of Original Envelope	Vertex Number of Simplified Envelope	Simplification Rate	Area of Original Envelope/km^2	Area of Simplified Envelope/km^2	Overall Error	Algebraic Error
17 May 2021	34,704	218	159	8216	8212	0.75%	−0.05%
6 June 2021	58,830	391	150	43,708	43,729	0.25%	0.05%
9 July 2021	101,881	602	169	42,501	42,558	0.42%	0.13%
5 August 2021	35,510	225	158	8615	8606	0.65%	−0.10%

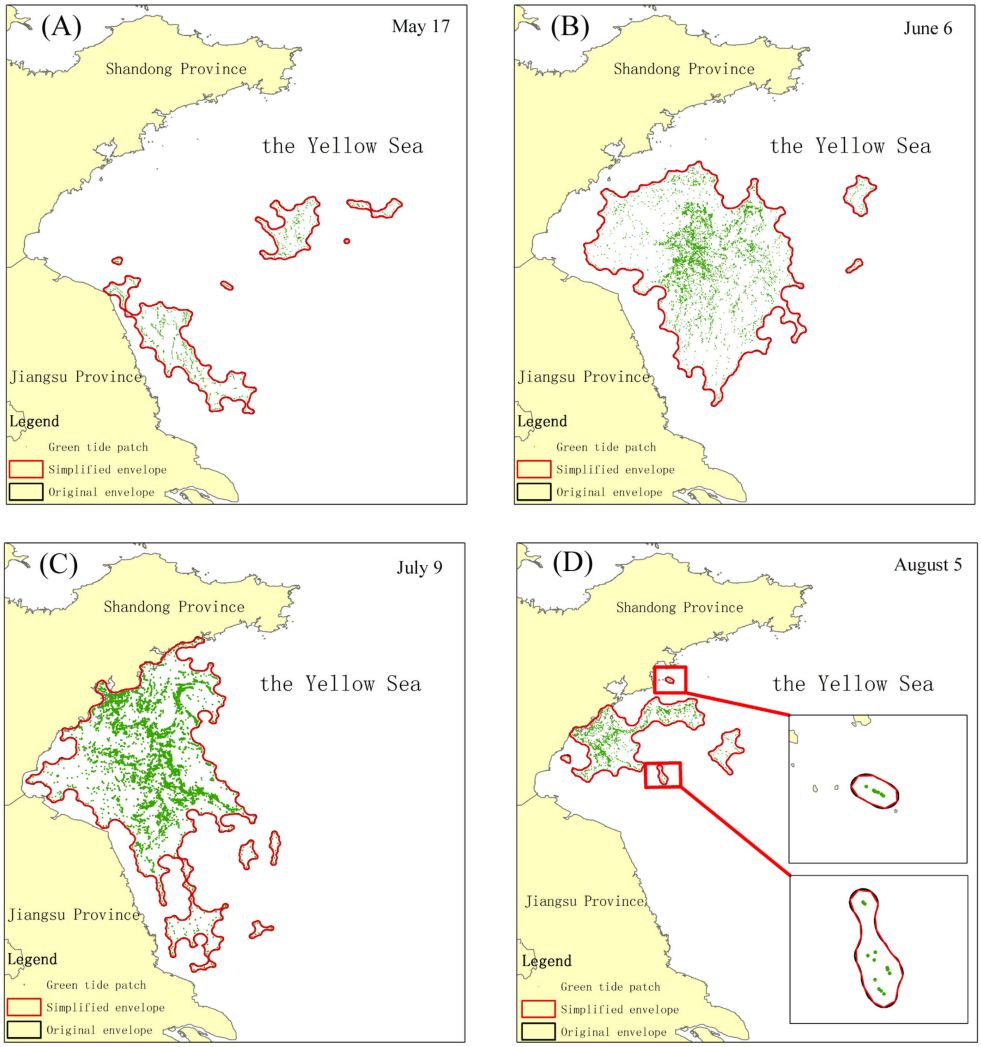

Figure 8. Simplified and original envelopes for 17 May (**A**), 6 June (**B**), 9 July (**C**), and 5 August (**D**) in 2021. The 5 August image zooms in some details of the envelope, showing a good fit between the simplified and original envelopes.

4.4. The Process of Green Tide Development and Drift

Using eight satellite images from 2021 (see Table 1), the green tide pixels were extracted using the method in Section 2.2.2. Then, the envelope of the green tide was obtained using the buffer analysis method. The green tide distribution areas for the eight dates were 387 km^2, 8217 km^2, 30,490 km^2, 43,709 km^2, 42,501 km^2, 24,834 km^2, 8615 km^2, and 1247 km^2, respectively. The corresponding daily green tide growth rates for the seven time periods were 1119 km^2/day, 2784 km^2/day, 1102 km^2/day, −37 km^2/day, −1963 km^2/day, −901 km^2/day, and −368 km^2/day, respectively. It can be seen from the above results that the green tide's distribution area went through rapid growth, faster growth, stabilization, a rapid decline, and a slow decline to disappearance. The eight envelopes clearly show the complete process of the green tide emergence—development—explosion—decline—disappearance (see Figure 9). It was detected in the Subei shoal on 10 May, and it proliferated for one month while drifting to the north, reaching its explosion stage on about 6 June, and then reached the south coast of Shandong. Around 9 July, the green tide entered the decline period, with the envelope area gradually decreasing until the green tide died out in late August [4,5].

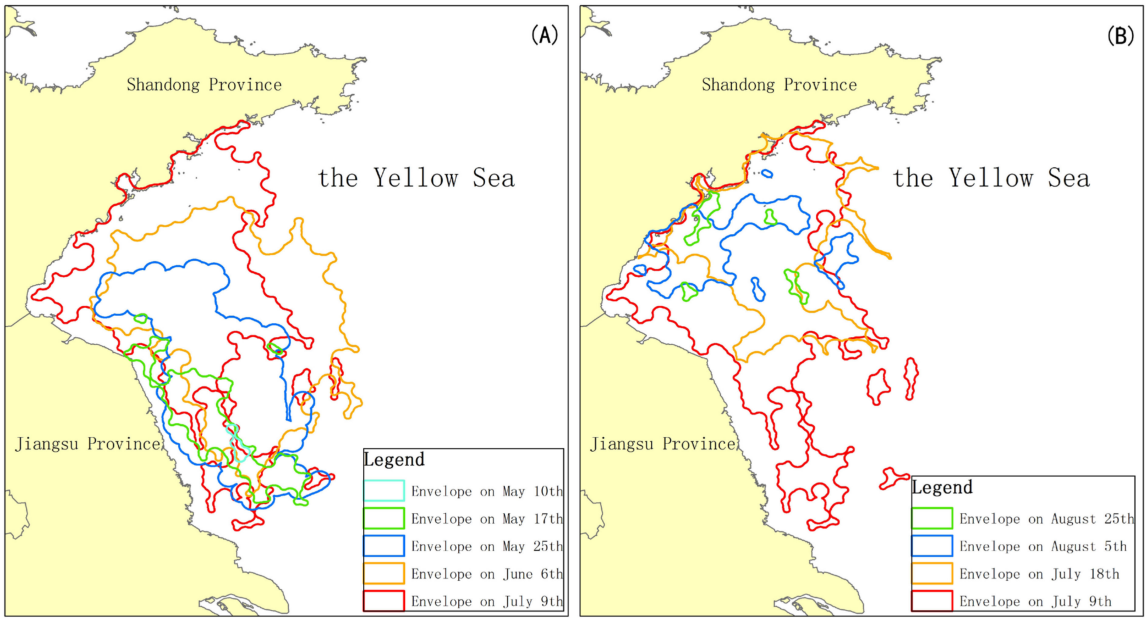

Figure 9. The whole process of green tide development and drift in 2021, where (**A**) shows the first half of the process, and (**B**) shows the second half.

5. Discussion

5.1. Side Lengths and Angles of the Distribution Envelope Simplified by SM-ADSL

The SM-ADSL method in this paper can simplify the number of boundary vertices of the original envelope to improve the prediction efficiency. The model was designed to simplify the distribution envelope by increasing the side lengths and changing the angles simultaneously. Here, we used the 17 May result as an example to analyze the side lengths and angles of the simplified distribution envelope using the SM-ADSL method (see Figure 10). Compared with the original side lengths and angles in Figure 3, the range of side lengths and angles changed significantly, with a more extensive range of angle values and much larger side lengths. Figure 8 shows that the side lengths range from 3 to 5 km and the angles range from 110 to 180°. The side lengths are mostly around 3 km when the angle is less than 140°, and the side lengths are mainly distributed around 4 km when the angle is 140°–180°. We can find that small side lengths correspond to small angles (large azimuth differences), and large side lengths corresponds to large angles (small azimuth differences), which is consistent with the side-angle relationship in the model.

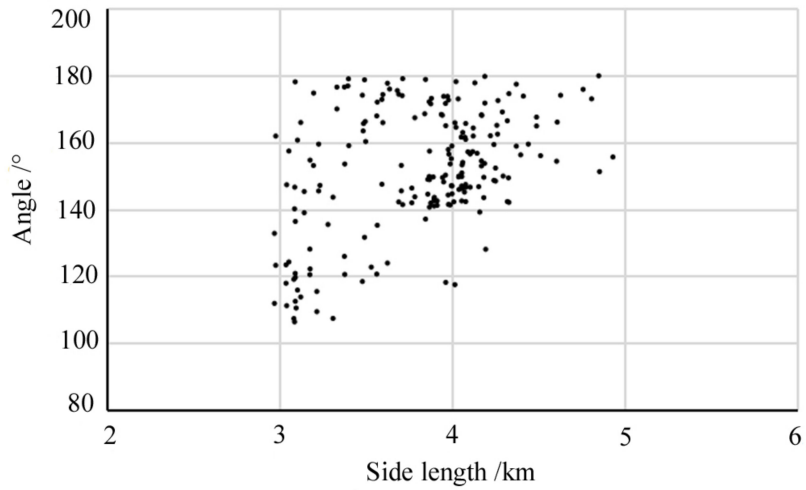

Figure 10. Side lengths and angles of green tide distribution envelope simplified by SM-ADSL on 17 May.

5.2. Comparison Analysis with the Existing Methods

The SM-ADSL method was compared with equidistance and Douglas–Peucker methods. The parameters for the equidistance and Douglas–Peucker methods were calculated according to the simplification rates of the four envelopes simplified by the SM-ADSL (shown in Table 2). The parameters of the equidistance method were 4.10 km, 4.22 km, 4.16 km, and 4.19 km for distribution envelopes from 17 May, 6 June, 9 July, and 5 August, respectively. The parameters for the Douglas–Peucker method were 0.48 km, 0.46 km, 0.515 km, and 0.48 km, respectively.

We compared and analyzed the advantages and disadvantages of the results produced by the method proposed in this paper with those of the equidistance and Douglas–Peucker methods in terms of qualitative and error analysis, using the results of 5 August (shown in Figure 11) as an example.

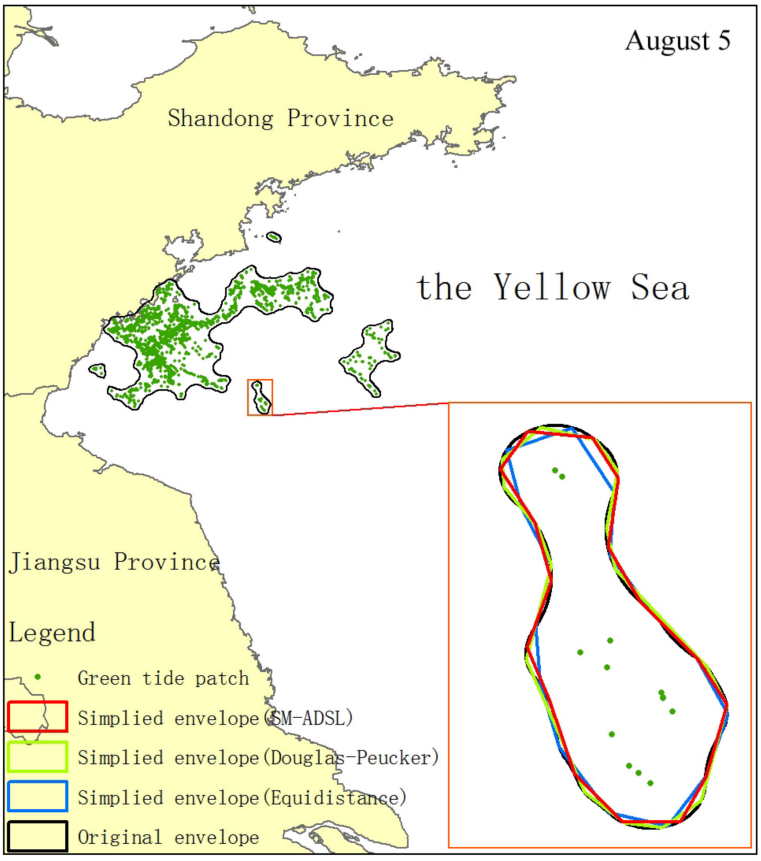

Figure 11. Comparison of the results of three simplification methods, SM-ADSL, equidistance, and Douglas–Peucker methods, for the 5 August distribution envelope.

Figure 11 shows that the equidistance method produced a simplified envelope (blue) that had a large deformation from the original envelope (black), especially in the high curvature part of the envelope, such as the top part of the magnified portion. In contrast, the results of the Douglas–Peucker [28,29,31] method and SM-ADSL were in better agreement with the original envelope.

Figure 12A shows that the SM-ADSL had a more minor algebraic error than the other two methods. The algebraic error of the Douglas–Peucker method was positive, which indicates that the area of the simplified envelope increased, and the algebraic error of the equidistance method was negative, which indicates that the area reduced after simplification. Figure 12B shows that the Douglas–Peucker method achieved the lowest overall error [29,31], while the SM-ADSL had little difference in overall error from the Douglas–Peucker method, and the equidistance method had the largest overall error. Based

on the above analysis of these two errors, the result shows that the method proposed in this paper is superior to the other two methods.

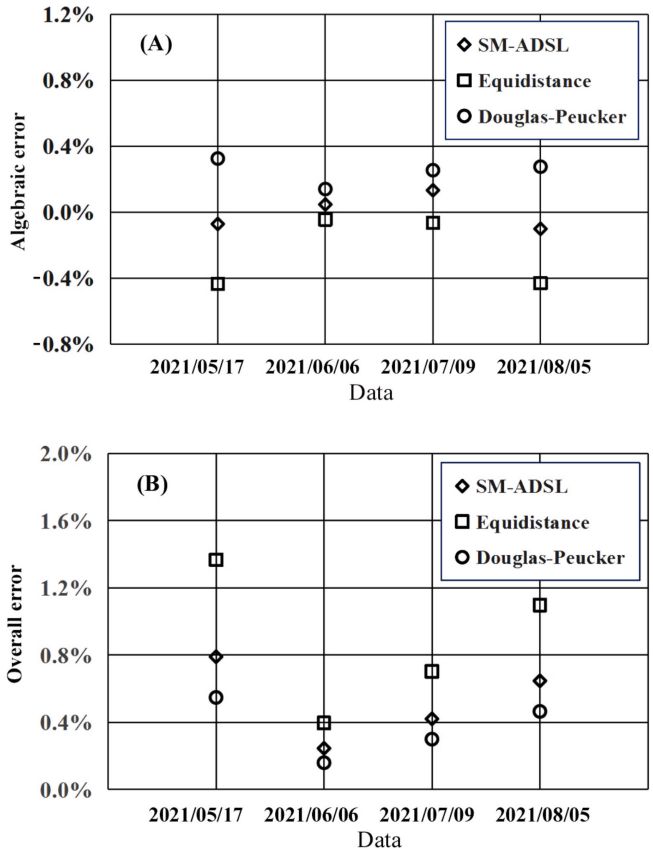

Figure 12. Errors produced by the SM-ADSL, Douglas–Peucker and equidistance methods: (**A**) algebraic errors, and (**B**) overall errors.

5.3. Drift Prediction Analysis

Huang Juan et al. [19,20,22] established the green tide drift prediction model based on the Lagrange particle tracking method. They integrated the model into an operational system called the remote sensing monitoring, forecasting, and early warning system of green tide disaster emergencies in the Yellow Sea. To specify the impact of simplification on prediction time, we calculated the 72 h drift prediction time of the four-phase distribution envelope before and after simplification. Figure 13 shows the predicted results of the distribution envelope on 6 June 2011. It can be found that the green tide generally moved to the northeast, which was consistent with the prevailing south wind in the Yellow Sea in summer as described in Section 2.1 [21,32], and that the green tide trajectory at point P was spiraling forward, which coincided with the regular semidiurnal tide at this point [47]. Table 3 shows that the time needed for simplified distribution envelope drift prediction was much shorter than without simplification. For example, for the green tide outbreak period on 9 July, the forecast time was shortened by 27 min, which can save time in making green tide disaster interception and removal plans. In the case of HY-1C with the transit time at 10:50, it takes about 3.5 h for data down-transmission, preprocessing, transmission to the user, green tide information extraction, and the drift prediction product production. At 13:50, the monitoring and forecast products could be transmitted to the field command department for emergency decision analysis. If the simplified method proposed in this paper were used, the product submission time would be about 13:20, half an hour earlier. Accordingly, the on-site interception and clearance would also be advanced by half an hour.

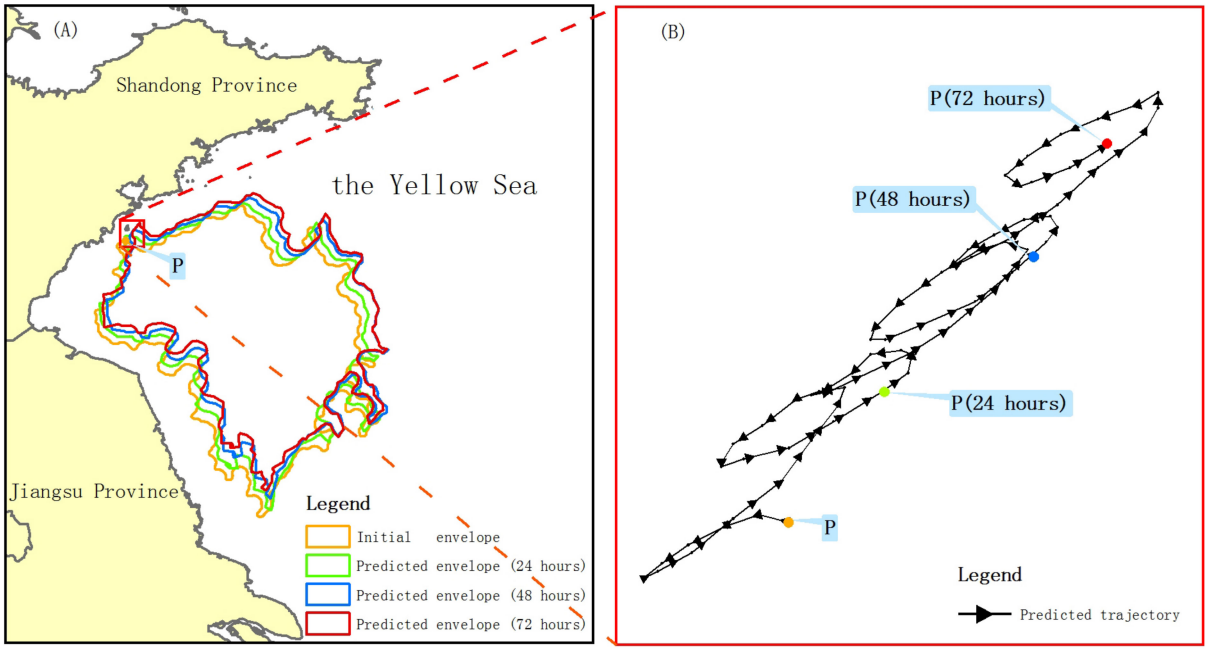

Figure 13. (**A**) Predicted drift of the green tide initial envelope on 6 June 2021 after 24, 48, and 72 h, and (**B**) green tide predicted trajectory of the 72 h drift at point P (shown as brown in both (**A**,**B**)), which is a vertex on the envelope.

Table 3. Drift prediction times for green tide distribution envelope before and after simplification.

Date	Before Simplification		After Simplification	
	Number of Vertices	Time Required	Number of Vertices	Time Required
17 May 2021	34,704	12 m and 56 s	218	1 m and 8 s
6 June 2021	58,830	20 m and 18 s	391	1 m and 51 s
9 July 2021	101,881	29 m and 45 s	602	2 m and 24 s
5 August 2021	35,510	12 m and 12 s	225	1 m and 10 s

The following should be noted: (1) Drift prediction experiments were conducted on the simplified envelopes of the other two methods, and it was found that the time required for prediction was consistent with the SM-ADSL. This indicates that the time needed for prediction depends on the number of remaining vertices after simplification. This result corresponds to the method used for green tide drift prediction, the Lagrangian particle method [19,48,49]. The prediction time for each particle is the same, so the number of particles determines the prediction calculation time. To avoid repetition, the time required for drift prediction by the other two methods was not listed. (2) The accuracy of the green tide predicted boundary mainly relies on the precision of wind, current, and drift prediction models. At the same time, a simplified boundary with minimal deformation also contributes to the accuracy of the predicted boundary. The evaluation of the predicted boundary's accuracy requires consideration of both the prediction model and continuous monitoring, which is beyond the main scope of this study and should be further explored in subsequent research.

5.4. The Impact of Monitoring Results from Different Satellite Sources on Decision-Making Plan Formulation

The detection capabilities of satellite images with different spatial resolutions vary [5,50–52]. This is because the monitored green tide information and distribution envelope will inevitably differ, and these differing monitoring results will necessarily impact the formulation of decision-making plans. To investigate the influence of different

image results on decision-making plans, this paper analyzes the monitoring results using quasi-synchronous HY-1C/D images with a resolution of 50 m and HJ-2A/B images with a resolution of 16 m (see Table 1). During the occurrence of green tide on 10 May, there were significant differences in the monitoring results of different resolution images. The 16 m resolution detected more green tide information than the 50 m resolution. This is because, during the occurrence stage, the green tide consists of small patches or thin, elongated strips along tidal channels, which the 50 m resolution images cannot detect [23]. On 6 June, during the outbreak stage of the green tide, the green tide had undergone sufficient growth, with larger patches and a wider range. The differences in the distribution area of the green tide were relatively small, with discrepancies mainly at the edge portions (see Figure 14). The figure shows two regions of difference, where it can be seen that the green tide signals in the discrepant regions are weak, and the colors are relatively light, making effective detection by the 50 m resolution HY-1 images difficult. This is because the northern green tide had undergone removal operations, with the residual green tide being relatively sparse and at the end of its growth cycle, resulting in low chlorophyll content and lighter color.

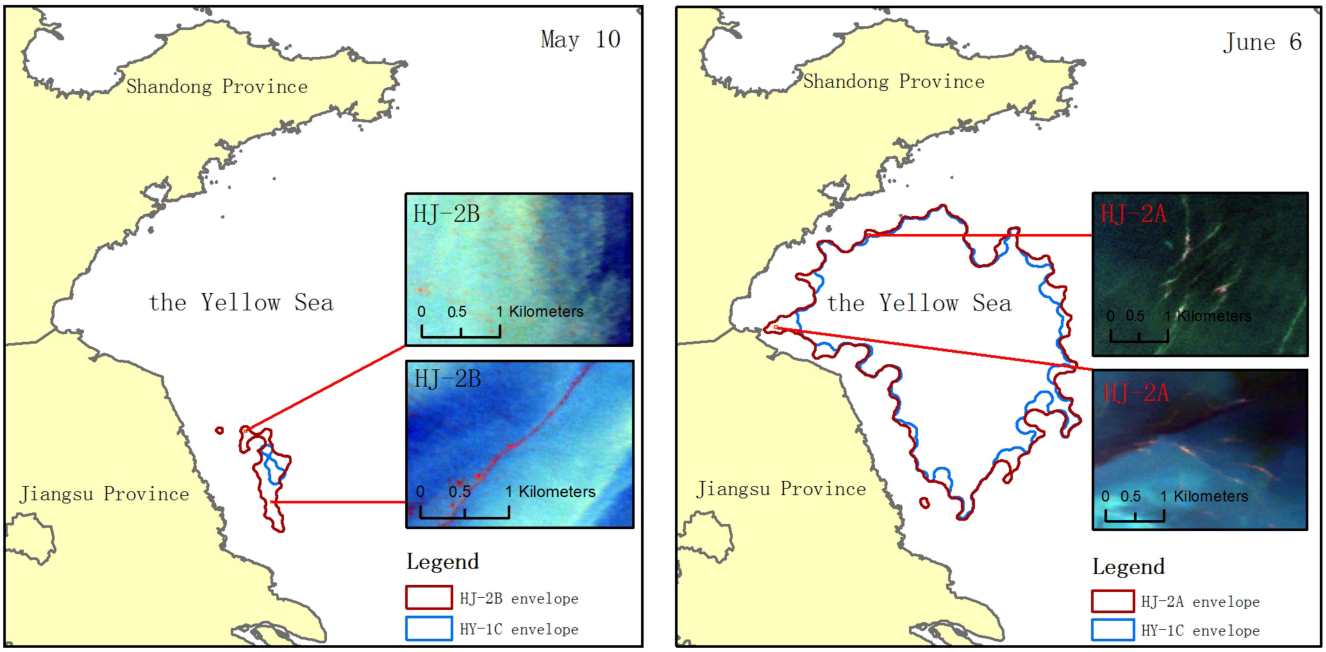

Figure 14. Comparison of distribution envelopes from satellite images with different spatial resolutions: The left image shows a comparison of distribution envelopes from the HY-1 satellite with a resolution of 50 m and the HJ-2 satellite with a resolution of 16 m on 10 May, while the right image shows a comparison of distribution envelopes on 6 June.

Overall, there are differences in the detection results of satellite images with different resolutions. High-resolution images provide more detailed monitoring, offering more comprehensive information and forming a larger distribution range. The monitoring differences vary with the date, especially during the early stage of the green tide when monitoring smaller patches shifts the outer edge line of the distribution envelope northward. When formulating emergency decision-making plans, harvesting areas based on the higher-resolution HJ-2 monitoring results will be biased towards the north, achieving the effect of early detection and early management. Therefore, it is recommended to formulate plans based on the monitoring results of higher-resolution satellite images during the early stage. During the outbreak stage, when the green tide has undergone sufficient growth and aggregation, the differences in green tide monitoring results between different resolutions are relatively small, and the impact on emergency decision-making for the green tide is also relatively minor.

6. Conclusions

The green tide distribution envelope and its prediction information are essential reference information in the decision-making of green tide disaster prevention and mitigation. We carried out research on the production of the envelope of green tide using remote sensing and geographic information analysis technology, and the main conclusions are as follows.

To address the issue of excessive vertices on the distributed envelope produced by buffer analysis, we proposed an envelope simplification model based on azimuth difference and side length (SM-ADSL) with a high simplification ratio and low deformation. The four-phase envelope simplification results showed that the simplification ratio was greater than 150, the algebraic error was less than 0.15%, and the overall error was less than 0.75%. Compared with the equidistance and Douglas–Peucker methods, SM-ADSL performs best in simplifying the distribution envelope, where SM-ADSL has the most minor algebraic error, while its overall error is similar to that of the Douglas–Peucker method and smaller than that of the equidistance method. Tests showed that using the simplified distribution envelope as the initial field for drift prediction significantly reduced the prediction time, thereby enhancing the efficiency of emergency decision-making for green tide disasters.

When using images with different spatial resolutions to extract the green tide and produce its distribution envelopes, we found that in the initial stage, due to the small size of green tide patches, high-resolution images can detect smaller patches, while lower-resolution marine images cannot detect these small patches, leading to significant differences in the distribution envelopes. In the development and outbreak stages, the green tide patches become larger after sufficient growth and aggregation, and the differences in distribution envelopes using images with different resolutions become smaller. Therefore, we recommend to use higher-resolution satellite images to detect green tides during their occurrence. This will ensure that even small patches are identified, providing more accurate information for early warning and decision-making.

The smoothness hypothesis of the distribution envelope in this paper is superior to manually delineated rigid envelopes. Smoothed envelopes enable the formation of standardized and uniform boundaries, which facilitate comparative analyses between different dates within the same year as well as comparisons of the same period across different years. Meanwhile, further research can be conducted on the mapping of envelopes, such as comprehensively considering the combined effects of green tide growth, surface wind fields, and ocean currents to form more realistic boundaries. When determining the buffer radius, the influence of shallow water depths and obstacles in nearshore areas could be taken into account, allowing for the setting of different buffer radii in different regions.

Author Contributions: Conceptualization, Y.D., G.H. and S.G.; methodology, Y.D.; software, Y.D.; validation, Y.D., G.H. and S.G.; formal analysis, Y.D.; investigation, Y.D.; resources, S.G.; data curation, Y.D.; writing—original draft preparation, Y.D.; writing—review and editing, G.H., Z.Y., Z.W., L.W., C.Y. and S.G.; visualization, Y.D.; supervision, G.H. and S.G.; project administration, L.W.; funding acquisition, L.W. and S.G. All authors have read and agreed to the published version of the manuscript.

Funding: This research was funded by the National Key Research and Development Program, China (grant no. 2022YFC3106005), and Shandong Provincial Key Laboratory of Marine Ecology and Environment & Disaster Prevention and Mitigation, China (grant no. 202208).

Data Availability Statement: The original contributions presented in the study are included in the article, further inquiries can be directed to the corresponding author.

Acknowledgments: The authors would like to thank the National Satellite Ocean Application Service for providing the HY-1C/D (CZI) images and the China Centre for Resources Satellite Data and Application for providing the HJ-2A/B(CCD) images.

Conflicts of Interest: The authors declare no conflicts of interest.

References

1. Sun, S.; Wang, F.; Li, C.; Qin, S.; Zhou, M.; Ding, L.; Pang, S.; Duan, D.; Wang, G.; Yin, B.; et al. Emerging challenges: Massive green algae blooms in the Yellow Sea. *Nat. Preced.* **2008**. [CrossRef]
2. Jiang, X.; Liu, J.; Zou, B.; Wang, Q.; Zeng, T.; Guo, M. The satellite remote sensing system used in emergency response monitoring for Entermorpha prolifera disaster and its application. *Acta Oceanol. Sin.* **2009**, *31*, 52–64.
3. Hu, C.; Li, D.; Chen, C.; Ge, J.; Muller Karger, F.E.; Liu, J.; Yu, F.; He, M.X. On the recurrent Ulva prolifera blooms in the Yellow Sea and East China Sea. *J. Geophys. Res. Ocean.* **2010**, *115*, C05017. [CrossRef]
4. Zhan, Y.; Qiu, Z.; Wang, Y.; Su, Y.; Li, Y.; Cui, Y.; Qu, S.; Wang, P.; Rong, X. Long-Term Spatiotemporal Characteristics of Ulva prolifera Green Tide and Effects of Environmental Drivers on Its Monitoring by Satellites: A Case Study in the Yellow Sea, China, from 2008 to 2023. *J. Mar. Sci. Eng.* **2024**, *12*, 630. [CrossRef]
5. Zheng, X.; Gao, Z.; Xu, F.; Ning, J.; Song, D.; Zheng, B. Study of remote sensing monitoring and comparison of green tide in the Yellow Sea based on VB-FAH index. *Mar. Sci.* **2017**, *41*, 71–79.
6. Li, D.; Gao, Z.; Song, D.; Shang, W.; Jiang, X. Characteristics and influence of green tide drift and dissipation in Shandong Rongcheng coastal water based on remote sensing. *Estuar. Coast. Shelf Sci.* **2019**, *227*, 106335. [CrossRef]
7. Li, D.; Gao, Z.; Zheng, X.; Wang, N. Analysis of the interannual variation characteristics of the northernmost drift position of the green tide in the Yellow Sea. *Environ. Sci. Pollut. Res.* **2020**, *27*, 35137–35147. [CrossRef]
8. Yi, D.; Juan, H.; Tingwei, C.; Zhenwen, W.; Yi, Z.; Conghua, C.; Chao, C.; Yanfang, X. The decomposition method of MODIS images Enteromorpha mixed pixels based on the relation of NDVI to abundance. *Haiyang Xuebao* **2015**, *37*, 123–131.
9. Ye, N.; Zhang, X.; Mao, Y.; Liang, C.; Xu, D.; Zou, J.; Zhuang, Z.; Wang, Q. 'Green tides' are overwhelming the coastline of our blue planet: Taking the world's largest example. *Ecol. Res.* **2011**, *26*, 477–485. [CrossRef]
10. Zhou, M.; Liu, D.; Anderson, D.M.; Valiela, I. Introduction to the Special Issue on green tides in the Yellow Sea. *Estuar. Coast. Shelf Sci.* **2015**, *163*, 3–8. [CrossRef]
11. Sun, M.; Li, Y.; Ren, Y.; Chen, Y. Redefine Sustainable Fisheries Targets Under the Impact of the Southern Yellow Sea Green Tide: Mitigating the Recurring Surge in Natural Mortality. *Front. Mar. Sci.* **2022**, *9*, 813024. [CrossRef]
12. Gu, X.F.; Chen, X.F.; Yin, Q.; Li, Z.Q.; Xu, H.; Shao, Y.; Li, Z.W. Stereoscopic Remote Sensing Used in Monitoring Enteromorpha Prolifra Disaster in Chinese Yellow Sea. *Spectrosc. Spectr. Anal.* **2011**, *31*, 1627.
13. Zou, Z.; Chen, C.; Liu, Z.; Zhang, Z.; Liang, J.; Chen, H.; Wang, L. Extraction of Aquaculture Ponds along Coastal Region Using U2-Net Deep Learning Model from Remote Sensing Images. *Remote Sens.* **2022**, *14*, 4001. [CrossRef]
14. Shi, W.; Wang, M. Green macroalgae blooms in the Yellow Sea during the spring and summer of 2008. *J. Geophys. Res. Atmos.* **2009**, *114*. [CrossRef]
15. Hu, C. A novel ocean color index to detect floating algae in the global oceans. *Remote Sens. Environ.* **2009**, *113*, 2118–2129. [CrossRef]
16. Son, Y.B.; Min, J.; Ryu, J. Detecting massive green algae (Ulva prolifera) blooms in the Yellow Sea and East China Sea using Geostationary Ocean Color Imager (GOCI) data. *Ocean Sci. J.* **2012**, *47*, 359–375. [CrossRef]
17. Xing, Q.; Hu, C. Mapping macroalgal blooms in the Yellow Sea and East China Sea using HJ-1 and Landsat data: Application of a virtual baseline reflectance height technique. *Remote Sens. Environ.* **2016**, *178*, 113–126. [CrossRef]
18. Zhang, H.; Sun, D.; Li, J.; Qiu, Z.; Wang, S.; He, Y. Remote Sensing Algorithm for Detecting Green Tide in China Coastal Waters Based on GF1-WFV and HJ-CCD Data. *Acta Opt. Sin.* **2016**, *36*, 28–36.
19. Huang, J.; Wu, L.J.; Gao, S.; Cao, Y.J.; Bai, T. Numerical simulation of emergency drift for green tide in the Yellow Sea. *Mar. Forecast.* **2011**, *28*, 25–32.
20. Wu, L.; Huang, J.; Ding, Y.; Liu, G.; Huang, S.; Gao, S.; Yuan, C.; Xu, J.; Wu, P.; Huang, R.; et al. Analysis on the causes of massive stranding of Yellow Sea green tide on Lianyungang and Rizhao coasts in 2022. *J. Oceanol. Limnol.* **2024**, *42*, 816–830. [CrossRef]
21. Wang, B.; Wu, L. Numerical Study on the Massive Outbreak of the Ulva prolifera Green Tides in the Southwestern Yellow Sea in 2021. *J. Mar. Sci. Eng.* **2021**, *9*, 1167. [CrossRef]
22. Cao, C.; Huang, J.; Gao, S.; Wu, L. *Remote Sensing Monitoring and Forecasting and Early Warning System for Yellow Sea Green Tide Disaster Emergency*; Ocean Press: Beijing, China, 2017.
23. Wang, Z.; Xiao, J.; Yuan, C.; Miao, X.; Fan, S.; Fu, M.; Xia, T.; Zhang, X. The drifting and spreading mechanism of floating Ulva mass in the waterways of Subei shoal, the Yellow Sea of China—Application for abating the world's largest green tides. *Mar. Pollut. Bull.* **2023**, *190*, 114789. [CrossRef] [PubMed]
24. Qi, L.; Hu, C.; Wang, M.; Shang, S.; Wilson, C. Floating Algae Blooms in the East China Sea. *Geophys. Res. Lett.* **2017**, *44*, 11501–11509. [CrossRef]
25. Ma, Y.; Wong, K.; Tsou, J.Y.; Zhang, Y. Investigating Spatial Distribution of Green-Tide in the Yellow Sea in 2021 Using Combined Optical and SAR Images. *J. Mar. Sci. Eng.* **2022**, *10*, 127. [CrossRef]
26. Douglas, D.H.; Peucker, T.K. Algorithms for the reduction of the number of points required to represent a digitized line or its caricature. *Cartogr. Int. J. Geogr. Inf. Geovis.* **1973**, *10*, 112–122. [CrossRef]
27. Mcmaster, R.B. Automated Line Generalization. *Cartogr. Int. J. Geogr. Inf. Geovis.* **1987**, *24*, 74–111. [CrossRef]
28. Saalfeld, A. Topologically Consistent Line Simplification with the Douglas-Peucker Algorithm. *Cartogr. Geogr. Inf. Sci.* **1999**, *26*, 7–18. [CrossRef]

29. Dal Santo, M.A.; de Oliveira, F.H.; Wosny, G.C. Algorithms for Automated Line Generalization in GIS. In Proceedings of the 28th Annual Esri User Conference, San Diego, CA, USA, 4–8 August 2008.
30. Wu, S.T.; Marquez, M.R.G. *A Non-Self-Intersection Douglas-Peucker Algorithm*; IEEE Computer Society: Sao Carlos, Brazil, 2003.
31. Li, Z.; Sui, H. An Integrated Technique for Automated Generalization of Contour Maps. *Cartogr. J.* **2000**, *37*, 29–37. [CrossRef]
32. Naimie, C.E.; Blain, C.A.; Lynch, D.R. Seasonal mean circulation in the Yellow Sea—A model-generated climatology. *Cont. Shelf Res.* **2001**, *21*, 667–695. [CrossRef]
33. Zhao, B.; Fang, G.; Cao, D. Numerical simulation of tide and tidal current in the Bohai, Yellow and East China Seas. *Acta Oceanol. Sin.* **1999**, *16*, 1–10.
34. Liu, A.; Yin, X.; Lu, M. The tide characteristics of the Huanghai Sea. *J. Oceanogr. Huanghai Bohai Seas* **1983**, *1*, 1–7.
35. Wu, H.; Xu, C.; Gao, X.; Ji, H. Research on high & low tide time error characteristics in the radial sand ridges area in North Jiangsu Province. *Mar. Sci. Bull.* **2016**, *35*, 163–169.
36. Jiang, X.; Gao, Z.; Zhang, Q.; Wang, Y.; Tian, X.; Shang, W.; Xu, F. Remote sensing methods for biomass estimation of green algae attached to nursery-nets and raft rope. *Mar. Pollut. Bull.* **2020**, *150*, 110678. [CrossRef] [PubMed]
37. Liu, D.; Keesing, J.K.; Xing, Q.; Shi, P. World's largest macroalgal bloom caused by expansion of seaweed aquaculture in China. *Mar. Pollut. Bull.* **2009**, *58*, 888–895. [CrossRef] [PubMed]
38. Liu, D.; Keesing, J.K.; Dong, Z.; Zhen, Y.; Di, B.; Shi, Y.; Fearns, P.; Shi, P. Recurrence of the world's largest green-tide in 2009 in Yellow Sea, China: Porphyra yezoensis aquaculture rafts confirmed as nursery for macroalgal blooms. *Mar. Pollut. Bull.* **2010**, *60*, 1423–1432. [CrossRef]
39. Wang, Z.; Xiao, J.; Fan, S.; Li, Y.; Liu, X.; Liu, D. Who made the world's largest green tide in China?—An integrated study on the initiation and early development of the green tide in Yellow Sea. *Limnol. Oceanogr.* **2015**, *60*, 1105–1117. [CrossRef]
40. Available online: http://www.nsoas.org.cn/news/content/2018-11/23/44_696.html (accessed on 23 November 2018).
41. Available online: https://zhuanlan.zhihu.com/p/686897019 (accessed on 13 March 2024).
42. Men, Y.; Liu, Y.; Ma, Y.; Wong, K.P.; Tsou, J.Y.; Zhang, Y. Remote Sensing Monitoring of Green Tide Disaster Using MODIS and GF-1 Data: A Case Study in the Yellow Sea. *J. Mar. Sci. Eng.* **2023**, *11*, 2212. [CrossRef]
43. Xu, S.; Yu, T.; Xu, J.; Pan, X.; Shao, W.; Zuo, J.; Yu, Y. Monitoring and Forecasting Green Tide in the Yellow Sea Using Satellite Imagery. *Remote Sens.* **2023**, *15*, 2196. [CrossRef]
44. Cao, Y.; Wu, Y.; Fang, Z.; Cui, X.; Liang, J.; Song, X. Spatiotemporal Patterns and Morphological Characteristics of Ulva prolifera Distribution in the Yellow Sea, China in 2016–2018. *Remote Sens.* **2019**, *11*, 445. [CrossRef]
45. Yuan, Y.B. Study of Daytime Sea Fog and Atmospheric Visibility over the Yellow Sea Based on GOCI Satellite Data. Ph.D. Thesis, Nanjing University of Information Science & Technology, Nanjing, China, 2017.
46. Zhang, S.; Xie, S.; Liu, Q.; Yang, Y.; Wang, X.; Ren, Z. Seasonal Variations of Yellow Sea Fog: Observations and Mechanisms. *J. Clim.* **2009**, *22*, 6758–6772. [CrossRef]
47. Cui, H.; Chen, J.; Jiang, X.; Fu, Y.; Qiao, F. A novel quantitative analysis for diurnal dynamics of Ulva prolifera patch in the Yellow Sea from Geostationary Ocean Color Imager observation. *Front. Mar. Sci.* **2023**, *10*, 1177997. [CrossRef]
48. Son, Y.B.; Choi, B.; Kim, Y.H.; Park, Y. Tracing floating green algae blooms in the Yellow Sea and the East China Sea using GOCI satellite data and Lagrangian transport simulations. *Remote Sens. Environ.* **2015**, *156*, 21–33. [CrossRef]
49. Bao, M.; Guan, W.; Yang, Y.; Cao, Z.; Chen, Q. Drifting trajectories of green algae in the western Yellow Sea during the spring and summer of 2012. *Estuar. Coast. Shelf Sci.* **2015**, *163*, 9–16. [CrossRef]
50. Cui, T.W.; Liang, X.J.; Gong, J.L.; Tong, C.; Xiao, Y.F.; Liu, R.J.; Zhang, X.; Zhang, J. Assessing and refining the satellite-derived massive green macro-algal coverage in the Yellow Sea with high resolution images. *ISPRS-J. Photogramm. Remote Sens.* **2018**, *144*, 315–324. [CrossRef]
51. Cui, T.; Zhang, J.; Sun, L.; Jia, Y.; Zhao, W.; Wang, Z.; Meng, J. Satellite monitoring of massive green macroalgae bloom (GMB): Imaging ability comparison of multi-source data and drifting velocity estimation. *Int. J. Remote Sens.* **2012**, *33*, 5513–5527. [CrossRef]
52. An, D.; Yu, D.; Zheng, X.; Zhou, Y.; Meng, L.; Xing, Q. Monitoring the Dissipation of the Floating Green Macroalgae Blooms in the Yellow Sea (2007–2020) on the Basis of Satellite Remote Sensing. *Remote Sens.* **2021**, *13*, 3811. [CrossRef]